Published in final edited form as:

Photochem Photobiol. 2022 March ; 98(2): 325–333. doi:10.1111/php.13544.

Ketone Incorporation Extends the Emission Properties of the Xanthene Scaffold Beyond 1000 nm†

Harrison C. Daly[1], **Siddharth S. Matikonda**[1], **Helena C. Steffens**[1], **Bastian Ruehle**[2], **Ute Resch-Genger**[2], **Joseph Ivanic**[3,*], **Martin J. Schnermann**[1,*]

[1]Chemical Biology Laboratory, Center for Cancer Research, National Cancer Institute, National Institutes of Health, Frederick, MD

[2]Division Biophotonics, Federal Institute of Materials Research and Testing (BAM),Berlin, Germany

[3]Advanced Biomedical Computational Science, Frederick National Laboratory for Cancer Research, Leidos Biomedical Research Inc., Frederick, MD

Abstract

Imaging in the shortwave-infrared region (SWIR, $\lambda = 1000 - 2500$ **nm**) has the potential to enable deep tissue imaging with high resolution. Critical to the development of these methods is the identification of low molecular weight, biologically compatible fluorescent probes that emit beyond 1000 nm. Exchanging the bridging oxygen atom on the xanthene scaffold (C10' position) with electron withdrawing groups has been shown to lead to significant redshifts in absorbance and emission. Guided by quantum chemistry computational modeling studies, we investigated the installation of a ketone bridge at the C10' position. This simple modification extends the absorbance maxima to 860 nm and the emission beyond 1000 nm, albeit with reduced photon output. Overall, these studies demonstrate that broadly applied xanthene dyes can be extended into the SWIR range.

INTRODUCTION

Fluorescence-based methods have transformed modern biological research. Shifting absorbance and emission to longer wavelengths reduces competitive excitation of biomolecules and light scattering - both of which can improve imaging quality. This has led to a concerted effort to identify long-wavelength emitting fluorophores for use in experiments ranging from cellular analysis to *in vivo* imaging (1,2). Recent efforts have shown that the shortwave infrared (SWIR, $\lambda = 1000 - 2500$ nm) or near-infrared II (NIR-II) region provides enhanced resolution and depth penetration in bulk tissue (3,4). Critical to the development of these methods was the availability of InGaAs detector-based cameras. These hardware developments have been complemented by significant progress in the design and synthesis of dyes that absorb and emit above 1000 nm (5–7). However, existing probes involve challenging multistep synthesis and exhibit low fluorescence quantum yields (8,9).

†This article is part of a Special Issue dedicated to the topic of Emerging Developments in Photocaging.

*Corresponding authors: joseph.ivanic@nih.gov (Joseph Ivanic), martin.schnermann@nih.gov (Martin J. Schnermann).

Overall, there remains a significant need for novel, biologically compatible, small-molecule fluorophores in this range.

Rhodamine and fluorescein dyes are important fluorophores and foundational components of many cellular imaging experiments. This is due to their excellent cell permeability, low toxicity and fluorogenic properties allowing for imaging cellular processes in real time (10). One strategy for extending the absorbance and emission maxima of these dyes involves extending the π-system, which can lead to an undesirable increase in hydrophobicity and molecular weight (11). Another more subtle strategy is to alter the C10' bridging atom of the xanthene scaffold (Fig. 1A). Prior reports have shown that modifying the bridging oxygen atom on the xanthene scaffold at the C10' position can lead to significant redshifts in absorbance and emission (12–23). In particular, recently reported phospho- and sulforhodamine derivatives have been reported with emission up to ~740 nm (Fig. 1A).

Here, we report the computational design, synthesis and initial analysis of xanthene derivatives substituted with a ketone at the C10' position. Across a series of known C10'-substituted systems, quantum chemical predictions of absorbance and emission maxima are in good agreement with experiment, and further calculations indicate that a ketone moiety would lead to a dramatic redshift. Additional analyses of the molecular orbitals involved in the electron excitations clearly demonstrate the link between substituent πelectronegativity and bathochromic shift. While a C10' ketone-substituted rhodamine had been described in a single report in the patent literature (24), no detailed information was available. Here, we report optimized syntheses of ketone-substituted xanthenes and rhodamines, as well as amide derivatives. Additionally, we detail that di-halogenated derivatives can undergo a bis-Heck reaction to provide pH-responsive exo-olefin derivatives. These synthetic efforts allowed key photophysical properties of these probes to be determined. Overall, these studies reveal the significant potential, as well as limitations, of these redshifted xanthene-based dyes as imaging agents in the SWIR range.

MATERIALS AND METHODS

Computational chemistry.

Quantum chemistry calculations were performed using a local version of the GAMESS package (25,26), where cc-pVTZ basis sets (spherical harmonics) were used throughout (27,28). Molecular orbitals were illustrated with MacMolPlt (29). Density functional theory (DFT) (30) and time-dependent density functional theory (TDDFT) (31–33) utilizing the B3LYP (34–36) functional were used to compute absorbance (S0 → S1*) and emission (S1 → S0*) (37) energies. The occupation restricted multiple active space (ORMAS) (38,39) method with second-order perturbation theory correction (ORMAS-PT2) (40) was also used to compute absorbance and emission energies at B3LYP and TDDFT-B3LYP optimized geometries respectively. ORMAS active spaces included all valence π-electrons and orbitals and state-averaged energies were optimized. Water-solvent effects were included in all calculations via the polarizable continuum model (PCM) (41–45) approach. Mulliken electron population analysis (46) was used to analyze the highest occupied molecular orbitals (HOMOs) and lowest unoccupied molecular orbitals (LUMOs). Full details and

results, including ORMAS active space partitioning scheme, are available in the Supporting Information.

Synthetic chemistry.

Detailed experimental procedures and characterization data are available in the Supporting Information.

Determination of molar absorption coefficients and fluorescence quantum yield of KR-1.

All spectroscopic measurements were carried out in duplicate at room temperature using 10 mm × 10 mm quartz cuvettes (Hellma GmbH) and high-purity spectroscopic grade solvents. High-purity water ($\sigma < 55$ μS) was obtained using a MilliPore filter system. Methanol (MeOH; Uvasol), Dimethylsulfoxide (DMSO; spectroscopic grade) and Dichloromethane (DCM; anhydrous) were purchased from Merck. The reference dye IR140 that was previously studied by us (47) was purchased from Lambda Physik.

Absorption measurements for the quantum yield determination were carried out on a calibrated absorption spectrometer Cary 5000 from Varian, Inc., using a step width of 1 nm, an integration time of 0.1 s and a spectral bandwidth of 2 nm. The absorbance spectra are corrected for blank absorption and scattering. The absorbance of the dye solutions used for fluorescence quantum yield determinations was generally kept below 0.1 to minimize dye aggregation and reabsorption effects for the measurements of the emission spectra and integral emission intensities (48).

Fluorescence emission measurements were performed with a calibrated spectrofluorometer FLS-920 from Edinburgh Photonics, equipped with a Xenon lamp, double monochromators, and a nitrogen-cooled PMT R5509P from Hamamatsu. A 550 nm cut-on filter was used in the excitation light path. The emission spectra were obtained by averaging 2 to 4 scans of the emission spectra (depending on the signal-to-noise ratio) with a step width of 1 nm, an integration time of 2 s and excitation and emission slit widths of 16 nm and 8 nm. Magic-angle conditions with the excitation and emission polarizers set to 0° and 54.7°, respectively, were employed to render the measured emission intensities independent of the emission anisotropy of the NIR emitter. All emission spectra were corrected for excitation intensity fluctuations using the signal of a reference detector as well as for blank emission and scattering by subtraction of the solvent spectra and for the wavelength dependence of the instrument's spectral responsivity utilizing a previously determined emission correction curve (48). The instrument was flushed with nitrogen during the measurements to avoid light absorption from atmospheric water (47).

The fluorescence quantum yield was determined relatively to the dye IR140 following a published procedure (48), the fluorescence quantum yield of which had been previously determined absolutely and relatively with different setups (49), and calculated according to the following equation:

$$\phi_x = \phi_{ref} \frac{F_x f_{ref}(\lambda_{ex,ref}) n_x^2}{F_{ref} f_x(\lambda_{ex,x}) n_{ref}^2}$$

where ϕ is the fluorescence quantum yield, F is the integral photon flux, f is the absorption factor at the excitation wavelength λ_{ex} and n is the refractive index of the solvent. The indices x and ref denote the sample and reference respectively. For the reference dye IR140, a fluorescence quantum yield of 0.20 in DMSO was used that was previously measured absolutely with a calibrated and validated integrating sphere setup (49). The absorption factor f at the excitation wavelength was obtained by averaging the absorption over the excitation bandwidth. The spectral width of the spectrofluorometer's excitation monochromator was not considered. An excitation wavelength of $\lambda_{ex} = 780$ nm was used for the dyes IR140 and KR-1. The refractive indices that were employed in the calculations were 1.479 for DMSO and 1.424 for DCM. The integrated photon fluxes required for the determination of the number of emitted photons were obtained in the wavelength ranges 970–1200 nm for KR-1 and IR140.

For additional details, including extinction coefficients, relative quantum yield measurements with KR-2 and KR-3 and details of the measurements taken in Fig. 2, see Section S5.

RESULTS AND DISCUSSION

Computational design

We first sought to identify the role of the central R-group fused at the C10' position in dimethylamino-xanthene-derived scaffolds (Fig. 1A). While our main goal was to identify a chemical modification that would significantly redshift absorbance and emission, we also sought to correlate spectroscopic properties with R-group electronic effects. We first computed absorbance and emission energies of the known series of systems **R1**-**R6** and the ketone derivative **R7** (Fig. 1C, Figure S4 and Table S4). We found the ORMAS-PT2-PCM(H_2O) method to be very reliable (absorbance/emission mean unsigned errors, MUEs, of 0.065/0.039 eV) and the TDDFT-B3LYP-PCM(H_2O) theory slightly less so (absorbance/emission MUEs of 0.397/0.167 eV). Importantly, both methods ranked the fluorophores in the correct order and, perhaps surprisingly, computed emission energies were generally more accurate than absorbance data. Most notably, the ketone derivative **R7** was predicted to absorb/emit above 800/900 nm—a dramatic bathochromic shift relative to other systems. As described below, this prediction was subsequently confirmed experimentally.

After verifying that all singlet states had predominant HOMO (π) → LUMO(π^*) characters (see SI for TDDFT-B3LYP-PCM excitation/deexcitation amplitudes), we further analyzed these orbitals. While HOMO structures and energies remain consistent across the series **R1**-**R7** (Fig. 1B,D), LUMO energies decrease substantially (by ~25 kcal mol^{-1}, Fig. 1D). The gradual change in LUMO character is visually apparent where C–C10' antibonding nodes are easily discernable for **R1** and **R2** but not for the other substituents that show a gradual extension of the bonding lobe to the C10' position for **R3 → R6** and beyond for **R7** (Fig. 1B). Indeed, quantified C–C10' bond orders in the LUMOs (Table S5) correlate very well with absorbance energies (Fig. 1E), thus rationalizing LUMO stabilization across the series. Furthermore, signed R-group LUMO electron populations (50) increase steadily across the series (Table S6) and show an excellent correlation with the absorbance energies

(Fig. 1F), indicating that excitation energies are lowered as the R-group π-electronegativity increases. In complete contrast, HOMO C-C10' bond orders and R-group populations are essentially zero throughout (Table S6). These observations can be reconciled by noting that: (1) HN− and O− substitutions add two electrons to the π-system, thus destabilizing the LUMO, (2) the other R-groups except OC—stabilize the LUMO by withdrawing some π-electron density and (3) OC—substitution adds two electrons and an empty antibonding π-orbital that the LUMO can extend into.

Computed TDDFT-B3LYP-PCM(H_2O) oscillator strengths rise steadily across the series **R1** → **R4**, but then suddenly decrease with the ketone derivative **R7** predicted to have the lowest absorption and emission intensities (Fig. 1G). Notably, this trend is confirmed experimentally with a strong correlation between oscillator strengths and absorption coefficients (Fig. 1 H), which includes the ketone-substituted compound detailed below. Further studies are needed to determine the origin of the trend between oscillator strengths and the C10' functional group—particularly for the design of brighter systems. While the computational chemistry results for the substituted series **R1**-**R7** are themselves illuminating, these studies clearly suggest that ketone substitution should yield a fluorophore with dramatically bathochromic-shifted absorption and emission bands.

Synthesis of keto-rhodamine (KR) dyes

Initial synthetic efforts focused on generating the parent ortho-methyl derivative **KR-1** using previously reported conditions (Scheme 1A) (24). We found that we could prepare **KR-1** in yields between 5% and 8% through the $AlCl_3$-promoted addition of **1** to 2-methylbenzoyl chloride. A screen of Lewis acids did not identify improved conditions. Although this reaction provided **KR-1**, it was difficult to purify and low yielding. Consequently, we considered alternative routes and were particularly inspired by a recent report by Lavis and coworkers that detailed the organolithium-mediated route to rhodamine derivatives (51). Building on this report, we developed the synthetic scheme shown in Scheme 1B, which could be used to generate **KR-1** in 25% yield over six steps. The synthesis started with methylation of bis(3-aminophenyl)methanone **6** with iodomethane in the presence of Cs_2CO_3 to give **1**. This was followed by regioselective bis-bromination alpha to the ketone bridge to generate dihalogenated **7**. The ketone **7** was reduced using $NaBH_4$ before subsequent alkylation to give a MOM (**2a**), Me (**2b**) and TBS (**2c**) protected intermediates **2a-c** respectively. These intermediates were screened for their ability to undergo lithiation and bisaddition to methyl 2-methylbenzoate. Both the MOM (**2a**) and Me (**2b**) protected compounds provided **3a** and **3b** in good yields of 58% and 54% respectively. Interestingly, the *t*-butyldimethylsilyl protected **2c** underwent transmetalation followed by silyl protecting group migration in a Retro-Brook-type rearrangement to give a organosilicon (C-Si) product (see Supporting Information for further details) (52). Upon deprotection using either TFA or BBr_3, **KR-1** could be accessed in 25% overall yield from the MOM protected **3a** or 22% for the Me **3b**, a ~ 3-fold improvement on the previously reported route.

Given the benefits of the late stage deprotection, the MOM-protected compound **2a** was chosen as our key intermediate. Phthalic anhydride underwent bis-aryl addition to generate **4** which remained as a ring-opened 9,10-anthracenediyl derivative until subsequent

deprotection with TFA to give ring-closed **KR-2** in 27% overall yield (Scheme 1B). We also set out to prepare a water-soluble "always on" amide derivative **KR** dye, as related probes have been described extensively in the rhodamine literature (53–60). The carboxylic acid **4** underwent amide coupling under standard conditions to give doubly protected intermediate **9**. Upon treatment with DDQ, **9** underwent MOM deprotection and *in situ* oxidation before standard *tert*-butyl ester deprotection with TFA in CH_2Cl_2 gave title compound **KR-3** in 18% yield over eight steps (Scheme 1). While TBS-protected dihalogenated **2c** was not suitable for Li-Br exchange and subsequent bis-addition, we hypothesized that it might undergo a palladium-mediated tandem Heck reaction with a protected acrylate species. Prior reports of similar chemistry have been applied to the generation of xanthene and anthracene derivatives from *o*, *o*'-dibromobiaryls with ethyl acrylate (61). However, to our knowledge this strategy has not been applied to generate rhodamine-based derivatives. Initially, methyl acrylate was chosen to screen reaction conditions and it was found employing Pd $(PPh_3)_4$, TEA and DMF at 150°C provided TBS-protected **10** in 40% yield (see Supporting Information). This product likely results from intermolecular Heck followed by an intramolecular Heck reaction to form the xanthene core. Deprotection was achieved using the mild conditions of ACN: H_2O: formic acid (2:1:0.05) to give exocyclic **11**. Upon subjecting **11** to an acidic environment (1:1 MeCN:H_2O w/1% formic acid), a longwavelength (λ_{max} = 870 nm) absorption band appeared (Figure S1). Encouraged by this result and in an effort to synthesize water-soluble conjugatable derivatives, compound **2c** was subjected to the same tandem-Heck ring-closing conditions with *tert*-butyl acrylate affording **5** in 71% yield (Scheme 1C). **5** underwent *tert*-butyl ester deprotection in TFA in CH_2Cl_2 and subsequent TSTU mediated activated ester formation before coupling with a heterobifunctional pegylated linker. Finally, using the same mild deprotection conditions of ACN: H_2O: formic acid (2:1:0.05), exocyclic **KR-4** could then be accessed in 63% yield from **5**.

Photophysical properties

Initial photophysical measurements concentrated on comparing the always-ON **KR-1** and **KR-3** to the parent ether-bridged reference dye tetramethylrosamine (**Ros**) (62). **KR-1** exhibited absorption (λ_{max}) and emission (λ_{em}) maxima of 862/1058 nm respectively (Table 1). This equates to bathochromic shifts in absorbance/emission of 313/488 nm relative to **Ros** in PBS. **KR-1** and **KR-3** showed similar λ_{max} and λ_{em} values in CH_2Cl_2 and a similarly pronounced redshift in λ_{em} of 1065 nm was observed for **KR-3** in PBS 7.4 (Table 1 and Fig. 2A–C). Notably, **KR-1** and **KR-3** exhibit significantly reduced absorption coefficients, which is in line with the computationally derived oscillator strengths (see above). The fluorescence quantum yields were determined to be 0.013 and 0.0031 in CH_2Cl_2, respectively, and were approximately two orders of magnitude lower in PBS. Therefore, this dramatic bathochromic shift in absorbance and emission is accompanied by significantly reduced photon output. This is to be expected according to the energy gap rule, which states that a smaller energy gap between S_1 and S_0 favors internal conversion relative to fluorescence (63). Thus, the reduced quantum yield is due to solvent-mediated nonradiative deactivation pathways—a feature also found in other SWIR dyes (4,8). Notably, however, previously reported cyanine-based SWIR probes maintain excellent

absorption coefficients (64–66). This leads to overall brighter dyes, with brightness defined as the product of the absorption coefficient at the excitation wavelength and quantum yield —a useful metric to determine the magnitude of the observable fluorescence signal.

In addition to conventional photon output, a useful feature of rhodamine dyes is their fluorogenic properties. Specifically, an equilibrium exists between a spirolactone “ring-closed,” nonfluorescent form and “ring-opened” fluorescent species (67,68). Having synthesized **KR-2** and **KR-4**, their fluorogenic switching properties were examined (Fig. 2D,G). In 5% TFA CH_2Cl_2, **KR-2** underwent ring opening as indicated by the increase in λ_{max} 848 nm and λ_{em} at 907 nm respectively. Notably, TFA was required to induce the appearance of the NIR absorption band and we could not identify other conditions that led to the ring-opened form.

An additional feature of certain xanthene derivatives is an exocyclic double bond (69,70). This was recently investigated by Johnsson and coworkers, where photoactivatable silicon rhodamines possessing an exocyclic alkene were generated through bisaryl lithium addition to glutaric anhydride (69). Our palladiummediated approach to **KR-4** provided a simple way to prepare ester-substituted exoalkenes. NMR studies of **KR-4** in 9:1 CD_3CN, D_2O revealed a proton singlet at 6.60 ppm which showed strong HSQC coupling to a CH unit at 119.5 ppm (see Supporting Information). Additionally, **KR-4** exhibits a λ_{abs} of 455 nm in PBS at pH 7. These results suggest that under neutral conditions, these compounds prefer the exoform. We hypothesized that acidic conditions might promote the conversion to an endoform, which would reestablish the long-wavelength optical properties of the xanthene core. In practice, we found that decreased pH led to the formation of new absorbance maxima λ_{abs} of 874 nm with a pK_a of 4.4 (Fig. 2E–G). These studies suggest this endo/exoisomerization chemistry can be used as a bioresponsive fluorogenic mechanism in the physiological pH range—an observation which may extend to other xanthene-based probes.

CONCLUSION

Here, we describe the longest emitting xanthene derivatives reported to date. This was achieved by the replacement of the ether bridge with a π-electron withdrawing ketone functional group on the xanthene core, leading to dramatic bathochromic shifts in absorbance and emission maxima. These studies demonstrate the significant impact of π-electron-withdrawing groups at this position on the electronic structure of the xanthene core. While carboxylic acid substituted **KR-2** remained in the nonfluorescent lactone form under biological conditions, their methyl and tertiary amine counterparts **KR-1** and **KR-3** exhibited large Stokes shifts and absorption and emission maxima that extend into the SWIR region at physiological pH. A fluorogenic exoolefin **KR-4** was synthesized and was shown to undergo an acid mediated exo–endo switching mechanism.

Broadly, these studies reveal that ketone substitution can have a dramatic effect on the absorption and emission maxima of xanthene dyes like rhodamines. However, the moderate absorption coefficients and quantum yields of these molecules need to be considered in the design of future strategies that seek to apply these probes. In this regard, we anticipate that

the low molecular weight of these molecules suggests that multimerization approaches have significant potential.

Supplementary Material

Refer to Web version on PubMed Central for supplementary material.

Acknowledgements—

This work was supported by the Intramural Research Program of the National Institutes of Health, National Cancer Institute, Center for Cancer Research. This project has been funded in whole or in part with Federal funds from the National Cancer Institute, National Institutes of Health, under Contract No. HHSN261200800001E. Dr. Sergey G. Tarasov and Ms. Marzena Dyba are thanked for use of instrumentation in the Biophysics Resource, CCR-NCI. UR gratefully acknowledges financial support by the German research council (DFG; project SIREN).

REFERENCES

1. Gorka AP, Nani RR and Schnermann MJ (2018) Harnessing cyanine reactivity for optical imaging and drug delivery. Acc. Chem. Res. 51, 3226–3235. [PubMed: 30418020]
2. Garland M, Yim JJ and Bogyo M (2016) A bright future for precision medicine: Advances in fluorescent chemical probe design and their clinical application. Cell Chem. Biol. 23, 122–136. [PubMed: 26933740]
3. Zhu B, Kwon S, Rasmussen JC, Litorja M and Sevick-Muraca EM (2020) Comparison of NIR versus SWIR fluorescence image device performance using working standards calibrated with SI units. IEEE Trans. Med. Imaging 39, 944–951. [PubMed: 31478842]
4. Thimsen E, Sadtler B and Berezin MY (2017) Shortwave-infrared (SWIR) emitters for biological imaging: A review of challenges and opportunities. Nanophotonics 6, 1043–1054.
5. Yuan L, Lin W, Zheng K, He L and Huang W (2013) Far-red to near infrared analyte-responsive fluorescent probes based on organic fluorophore platforms for fluorescence imaging. Chem. Soc. Rev. 42, 622–661. [PubMed: 23093107]
6. Wan H, Yue J, Zhu S, Uno T, Zhang X, Yang Q, Yu K, Hong G, Wang J, Li L, Ma Z, Gao H, Zhong Y, Su J, Antaris AL, Xia Y, Luo J, Liang Y and Dai H (2018) A bright organic NIR-II nanofluorophore for three-dimensional imaging into biological tissues. Nat. Commun. 9, 1171. [PubMed: 29563581]
7. Zhu S, Tian R, Antaris AL, Chen X and Dai H (2019) Nearinfrared-II molecular dyes for cancer imaging and surgery. Adv. Mater. 31, 1900321.
8. Friedman HC, Cosco ED, Atallah TL, Jia S, Sletten EM and Caram JR (2021) Establishing design principles for emissive organic SWIR chromophores from energy gap laws. ChemRxiv. 10.26434/chemrxiv.14374493.v1
9. Cao J, Zhu B, Zheng K, He S, Meng L, Song J and Yang H (2019) Recent progress in NIR-II contrast agent for biological imaging. Front. Bioeng. Biotechnol. 7, 487. [PubMed: 32083067]
10. Lavis LD (2017) Teaching old dyes new tricks: Biological probes built from fluoresceins and rhodamines. Annu. Rev. Biochem. 86, 825–843. [PubMed: 28399656]
11. Wiktorowski S, Rosazza C, Winterhalder MJ, Daltrozzo E and Zumbusch A (2014) Water-soluble pyrrolopyrrole cyanine (PPCy) NIR fluorophores. Chem. Commun. 50, 4755–4758.
12. Fu M, Xiao Y, Qian X, Zhao D and Xu Y. (2008) A design concept of long-wavelength fluorescent analogs of rhodamine dyes: Replacement of oxygen with silicon atom. Chem. Commun. 1780–1782. 10.1039/b718544h
13. Koide Y, Urano Y, Hanaoka K, Terai T and Nagano T (2011) Evolution of group 14 rhodamines as platforms for near-infrared fluorescence probes utilizing photoinduced electron transfer. ACS Chem. Biol. 6, 600–608. [PubMed: 21375253]
14. Grimm JB, Sung AJ, Legant WR, Hulamm P, Matlosz SM, Betzig E and Lavis LD (2013) Carbofluoresceins and carborhodamines as scaffolds for high-contrast fluorogenic probes. ACS Chem. Biol. 8, 1303–1310. [PubMed: 23557713]

15. Chai X, Cui X, Wang B, Yang F, Cai Y, Wu Q and Wang T (2015) Near-infrared phosphorus-substituted rhodamine with emission wavelength above 700 nm for bioimaging. Chem. A. Eur. J. 21, 16754–16758. 10.1002/chem.201502921
16. Grimm JB, Gruber TD, Ortiz G, Brown TA and Lavis LD (2016) Virginia orange: A versatile, red-shifted fluorescein scaffold for single- and dual-input fluorogenic probes. Bioconjug. Chem. 27, 474–480. [PubMed: 26636613]
17. Zhou X, Lai R, Beck JR, Li H and Stains CI (2016) Nebraska Red: a phosphinate-based near-infrared fluorophore scaffold for chemical biology applications. Chem. Commun. 52, 12290–12293.
18. Fang Y, Good GN, Zhou X and Stains CI (2019) Phosphinate-containing rhodol and fluorescein scaffolds for the development of bioprobes. Chem. Commun. 55, 5962–5965.
19. Fukazawa A, Suda S, Taki M, Yamaguchi E, Grzybowski M, Sato Y, Higashiyama T and Yamaguchi S (2016) Phospha-fluorescein: A red-emissive fluorescein analogue with high photobleaching resistance. Chem. Commun. 52, 1120–1123.
20. Liu J, Sun Y-Q, Zhang H, Shi H, Shi Y and Guo W (2016) Sulfone-rhodamines: A new class of near-infrared fluorescent dyes for bioimaging. ACS Appl. Mater. Interfaces. 8, 22953–22962. [PubMed: 27548811]
21. Ando N, Soutome H and Yamaguchi S (2019) Near-infrared fluorescein dyes containing a tricoordinate boron atom. Chem. Sci. 10, 7816–7821. [PubMed: 31588332]
22. Lei Z, Li X, Luo X, He H, Zheng J, Qian X and Yang Y (2017) Bright, stable, and biocompatible organic fluorophores absorbing/emitting in the deep near-infrared spectral region. Angew. Chem. Int. Ed. 56, 2979–2983.
23. Zhang X, Chen L, Huang Z, Ling N and Xiao Y (2021) Cycloketal xanthene dyes: A new class of near-infrared fluorophores for super-resolution imaging of live cells. Chem. A. Eur. J. 27, 3688–3693.
24. Sawano B, Sasaki N & Matsumoto M (1994) Preparation of spiro [anthrone-phthalide] derivatives for recording materials. Vol. JP 06234757. pp. 18 pp. Mitsui Toatsu Chemicals, Japan; Yamamoto Chemicals Inc., Japan.
25. Schmidt MW, Baldridge KK, Boatz JA, Elbert ST, Gordon MS, Jensen JH, Koseki S, Matsunaga N, Nguyen KA, Su SJ, Windus TL, Dupuis M and Montgomery JA (1993) General atomic and molecular electronic-structure system. J. Comput. Chem. 14, 1347–1363. 10.1002/jcc.540141112
26. Barca GMJ, Bertoni C, Carrington L, Datta D, De Silva N, Deustua JE, Fedorov DG, Gour JR, Gunina AO, Guidez E, Harville T, Irle S, Ivanic J, Kowalski K, Leang SS, Li H, Li W, Lutz JJ, Magoulas I, Mato J, Mironov V, Nakata H, Pham BQ, Piecuch P, Poole D, Pruitt SR, Rendell AP, Roskop LB, Ruedenberg K, Sattasathuchana T, Schmidt MW, Shen J, Slipchenko L, Sosonkina M, Sundriyal V, Tiwari A, Vallejo JLG, Westheimer B, Wloch M, Xu P, Zahariev F and Gordon MS (2020) Recent developments in the general atomic and molecular electronic structure system. J. Chem. Phys. 152, 154102. [PubMed: 32321259]
27. Dunning TH (1989) Gaussian-basis sets for use in correlated molecular calculations. 1. The atoms boron through neon and hydrogen. J. Chem. Phys. 90, 1007–1023.
28. Dunning TH, Peterson KA and Wilson AK (2001) Gaussian basis sets for use in correlated molecular calculations. X. The atoms aluminium through argon revisited. J. Chem. Phys. 114, 9244–9253.
29. Bode BM and Gordon MS (1998) MacMolPlt: A graphical user interface for GAMESS. J. Mol. Graph. Model. 16, 133–138. [PubMed: 10434252]
30. Kohn W and Sham LJ (1965) Self-consistent equations including exchange and correlation effects. Phys. Rev. 140, 1133–2000.
31. Runge E and Gross EKU (1984) Density-functional theory for time-dependent systems. Phys. Rev. Lett. 52, 997–1000. 10.1103/PhysRevLett.52.997
32. Gross EKU & Kohn W (1990) Time-dependent density-functional theory. In Advances in Quantum Chemistry, Vol. 21. pp. 225–291. https://www.sciencedirect.com/science/article/pii/S0065327608606000
33. van Leeuwen R (2001) Key concepts in time-dependent density-functional theory. Int. J. Mod. Phys. B 15, 1969–2023.

34. Becke AD (1993) Density-functional thermochemistry. 3. The role of exact exchange. J. Chem. Phys 98, 5648–5652.
35. Stephens PJ, Devlin FJ, Chabalowski CF and Frisch MJ (1994) Ab-initio calculation of vibrational absorption and circular-dichroism spectra using density-functional force-fields. J. Phys. Chem. 98, 11623–11627.
36. Hertwig RH and Koch W (1997) On the parameterization of the local correlation functional. What is Becke-3-LYP? Chem. Phys. Lett. 268, 345–351. https://www.sciencedirect.com/science/article/pii/S0009261497002078?via%3Dihub
37. Chiba M, Tsuneda T and Hirao K (2006) Excited state geometry optimizations by analytical energy gradient of long-range corrected time-dependent density functional theory. J. Chem. Phys. 124, 144106. [PubMed: 16626179]
38. Ivanic J (2003) Direct configuration interaction and multiconfigurational self-consistent-field method for multiple active spaces with variable occupations. I. Method. J. Chem. Phys. 119, 9364–9376.
39. Ivanic J (2003) Direct configuration interaction and multiconfigurational self-consistent-field method for multiple active spaces with variable occupations. II. Application to oxoMn(salen) and N2O4. J. Chem. Phys. 119, 9377–9385.
40. Roskop L and Gordon MS (2011) Quasi-degenerate second-order perturbation theory for occupation restricted multiple active space self-consistent field reference functions. J. Chem. Phys. 135. 10.1063/1.3609756
41. Miertus S, Scrocco E and Tomasi J (1981) Electrostatic interaction of a solute with a continuum – A direct utilization of abinitio molecular potentials for the prevision of solvent effects. Chem. Phys. 55, 117–129.
42. Li H and Jensen JH (2004) Improving the efficiency and convergence of geometry optimization with the polarizable continuum model: New energy gradients and molecular surface tessellation. J. Comput. Chem. 25, 1449–1462. [PubMed: 15224389]
43. Tomasi J, Mennucci B and Cammi R (2005) Quantum mechanical continuum solvation models. Chem. Rev. 105, 2999–3093. [PubMed: 16092826]
44. Li H (2009) Quantum mechanical/molecular mechanical/continuum style solvation model: Linear response theory, variational treatment, and nuclear gradients. J. Chem. Phys. 131, 184103. [PubMed: 19916594]
45. Wang YL and Li H (2010) Excited state geometry of photoactive yellow protein chromophore: A combined conductorlike polarizable continuum model and time-dependent density functional study. J. Chem. Phys. 133, 34108.
46. Mulliken RS (1955) Electronic Population Analysis on Lcao-Mo Molecular Wave Functions. 1. J. Chem. Phys. 23, 1833–1840.
47. Hatami S, Würth C, Kaiser M, Leubner S, Gabriel S, Bahrig L, Lesnyak V, Pauli J, Gaponik N, Eychmuller A and Resch-Genger U (2015) Absolute photoluminescence quantum yields of IR26 and IR-emissive Cd1–xHgxTe and PbS quantum dots – method- and material-inherent challenges. Nanoscale 7, 133–143. [PubMed: 25407424]
48. Würth C, Grabolle M, Pauli J, Spieles M and Resch-Genger U (2013) Relative and absolute determination of fluorescence quantum yields of transparent samples. Nat. Protoc. 8, 1535–1550. [PubMed: 23868072]
49. Hatami S, Wurth C, Kaiser M, Leubner S, Gabriel S, Bahrig L, Lesnyak V, Pauli J, Gaponik N, Eychmuller A and Resch-Genger U (2015) Absolute photoluminescence quantum yields of IR26 and IR-emissive Cd(1–x)Hg(x)Te and PbS quantum dots–method- and material-inherent challenges. Nanoscale 7, 133–143. https://pubs.rsc.org/en/content/articlelanding/2015/nr/c4nr04608k [PubMed: 25407424]
50. Matikonda SS, Ivanic J, Gomez M, Hammersley G and Schnermann MJ (2020) Core remodeling leads to long wavelength fluoro-coumarins. Chem. Sci. 11, 7302–7307. [PubMed: 34123014]
51. Grimm JB, Brown TA, Tkachuk AN and Lavis LD (2017) General synthetic method for Si-fluoresceins and Si-rhodamines. ACS Central Sci. 3, 975–985.
52. Bariak V, Malastová A, Almássy A and Šebesta R (2015) Retro-brook rearrangement of ferrocene-derived silyl ethers. Chem. A Eur. J. 21, 13445–13453.

53. Deal PE, Liu P, Al-Abdullatif SH, Muller VR, Shamardani K, Adesnik H and Miller EW (2020) Covalently tethered rhodamine voltage reporters for high speed functional imaging in brain tissue. J. Am. Chem. Soc. 142, 614–622. [PubMed: 31829585]
54. Deal PE, Kulkarni RU, Al-Abdullatif SH and Miller EW(2016) Isomerically pure tetramethylrhodamine voltage reporters. J. Am. Chem. Soc. 138, 9085–9088. [PubMed: 27428174]
55. Homma M, Takei Y, Murata A, Inoue T and Takeoka S (2015) A ratiometric fluorescent molecular probe for visualization of mitochondrial temperature in living cells. Chem. Commun. 51, 6194–6197.
56. Okorochenkova Y, Porubský M, Benická S and Hlaváč J (2018) A novel three-fluorophore system as a ratiometric sensor for multiple protease detection. Chem. Commun. 54, 7589–7592.
57. Minoshima M, Kikuta J, Omori Y, Seno S, Suehara R, Maeda H, Matsuda H, Ishii M and Kikuchi K (2019) In vivo multicolor imaging with fluorescent probes revealed the dynamics and function of osteoclast proton pumps. ACS Central Sci. 5, 1059–1066.
58. Sibbersen C, Palmfeldt J, Hansen J, Gregersen N, Jørgensen KA and Johannsen M (2013) Development of a chemical probe for identifying protein targets of α-oxoaldehydes. Chem. Commun. 49, 4012–4014. https://pubs.rsc.org/en/content/articlelanding/2013/cc/c3cc41099d
59. Yan R, Sander K, Galante E, Rajkumar V, Badar A, Robson M, El-Emir E, Lythgoe MF, Pedley RB and Årstad E (2013) A one-pot three-component radiochemical reaction for rapid assembly of 125I-labeled molecular probes. J. Am. Chem. Soc. 135, 703–709. [PubMed: 23194416]
60. Kolmakov K, Hebisch E, Wolfram T, Nordwig LA, Wurm CA, Ta H, Westphal V, Belov VN and Hell SW (2015) Farred emitting fluorescent dyes for optical nanoscopy: fluorinated silicon-rhodamines (SiRF dyes) and phosphorylated oxazines. Chem. A. Eur J. 21, 13344–13356.
61. Prashad M, Liu Y, Mak XY, Har D, Repič O and Blacklock TJ (2002) Double Heck reaction of bridged o, o′-dibromobiaryls with ethyl acrylate. Tetrahedron Lett. 43, 8559–8562. https://www.sciencedirect.com/science/article/pii/S0040403902020907
62. Zhou X, Lesiak L, Lai R, Beck JR, Zhao J, Elowsky CG, Li H and Stains CI (2017) Chemoselective alteration of fluorophore scaffolds as a strategy for the development of ratiometric chemodosimeters. Angew. Chem. Int. Ed. 56, 4197–4200.
63. Lakowicz JR (2006) Principles of fluorescence spectroscopy, 3rd ed.; Springer Science+Business Media, LLC, New York.
64. Cosco ED, Caram JR, Bruns OT, Franke D, Day RA, Farr EP, Bawendi MG and Sletten EM (2017) Flavylium polymethine fluorophores for near- and shortwave infrared imaging. Angew. Chem. 56, 13126–13129. [PubMed: 28806473]
65. Li B, Lu L, Zhao M, Lei Z and Zhang F (2018) An efficient 1064 nm NIR-II excitation fluorescent molecular dye for deeptissue high-resolution dynamic bioimaging. Angew. Chem. 57, 7483–7487. [PubMed: 29493057]
66. Cosco ED, Spearman AL, Ramakrishnan S, Lingg JGP, Saccomano M, Pengshung M, Arus BA, Wong KCY, Glasl S, Ntziachristos V, Warmer M, McLaughlin RR, Bruns OT and Sletten EM (2020) Shortwave infrared polymethine fluorophores matched to excitation lasers enable non-invasive, multicolour in vivo imaging in real time. Nat. Chem. 12, 1123–1130. [PubMed: 33077925]
67. Grimm JB, English BP, Chen J, Slaughter JP, Zhang Z, Revyakin A, Patel R, Macklin JJ, Normanno D, Singer RH, Lionnet T and Lavis LD (2015) A general method to improve fluorophores for live-cell and single-molecule microscopy. Nat. Methods 12, 244–250. [PubMed: 25599551]
68. Zheng Q, Ayala AX, Chung I, Weigel AV, Ranjan A, Falco N, Grimm JB, Tkachuk AN, Wu C, Lippincott-Schwartz J, Singer RH and Lavis LD (2019) Rational design of fluorogenic and spontaneously blinking labels for super-resolution imaging. ACS Central Sci. 5, 1602–1613.
69. Frei MS, Hoess P, Lampe M, Nijmeijer B, Kueblbeck M, Ellenberg J, Wadepohl H, Ries J, Pitsch S, Reymond L and Johnsson K (2019) Photoactivation of silicon rhodamines via a light-induced protonation. Nat. Commun. 10, 4580. [PubMed: 31594948]
70. Horváth P, Šebej P, Kovář D, Damborský J, Prokop Z and Klán P (2019) Fluorescent pH indicators for neutral to near-alkaliné conditions based on 9-iminopyronin derivatives. ACS Omega 4, 5479–5485.

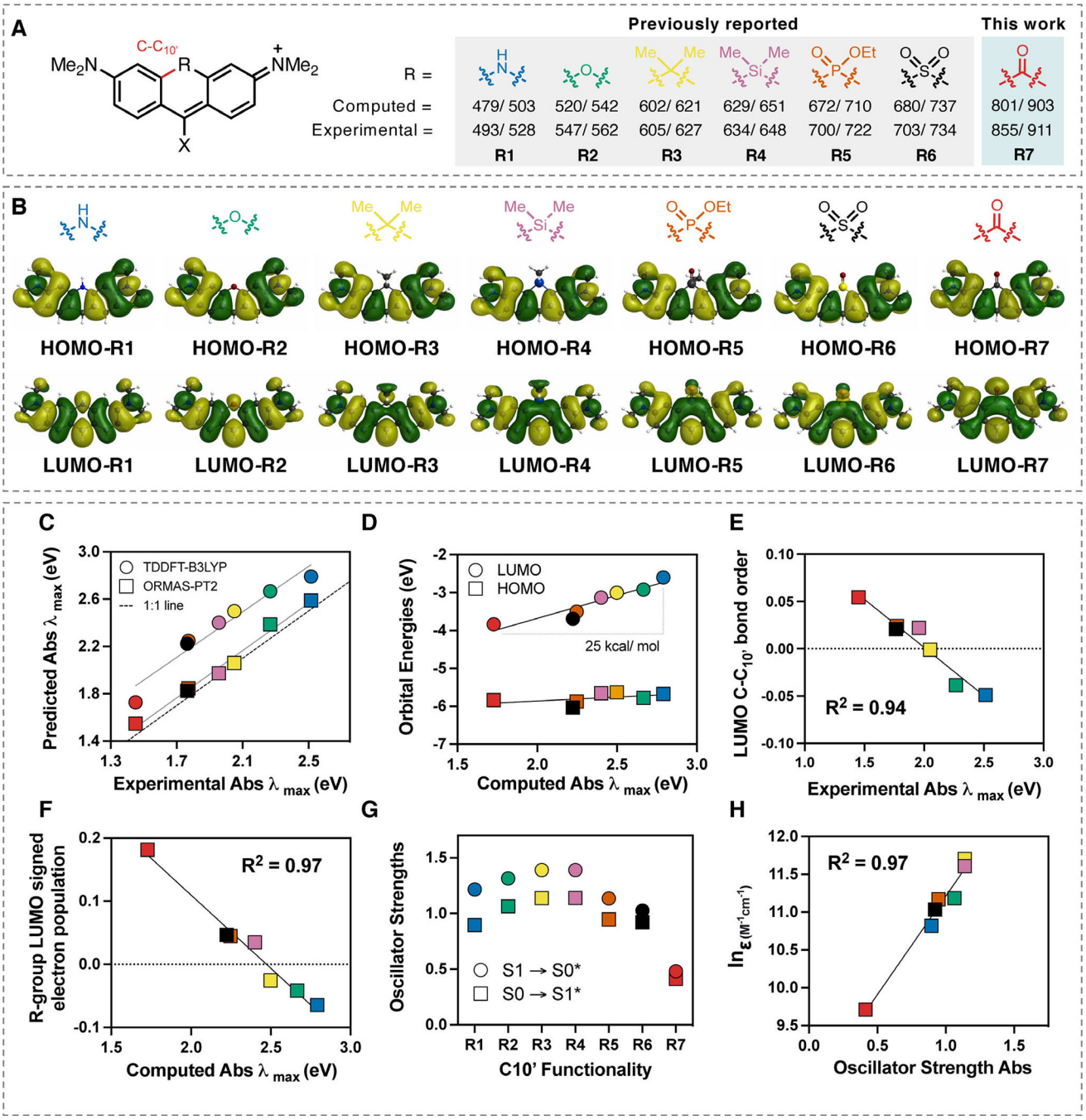

Figure 1.

(A) Computational and experimental absorbance/emission maxima data for substituents (1–7) at R-position on a dimethylamino-xanthene-derived scaffold (see Table S1 for X-group substituent). (B) Comparisons between the HOMOs and LUMOs of R1-R7. (C) Correlation between experimental and predicted λ_{max} absorbance using TDDFT-B3LYP-PCM(H_2O) and ORMAS-PT2-PCM(H_2O). (D) Correlation between the computed λ_{max} absorbance (TDDFT-B3LYP-PCM(H_2O)) and HOMO/LUMO orbital energies. (E) Correlation ($R^2 = 0.94$) between experimental λ_{max} absorbance and C–C10' bond order in the LUMO. (F) Correlation

($R^2 = 0.97$) between signed R-group Mulliken population in LUMO and computed λ_{max} absorbance. (G) Comparison between computed absorbance and emission oscillator strengths (TDDFT-B3LYP-PCM(H_2O)) for R1-R7. H) Comparison between computed absorbance oscillator strengths (TDDFT-B3LYP-PCM(H_2O)) for R1-R7 and experimental extinction coefficient values for structurally related compounds (see Supporting Information for further details).

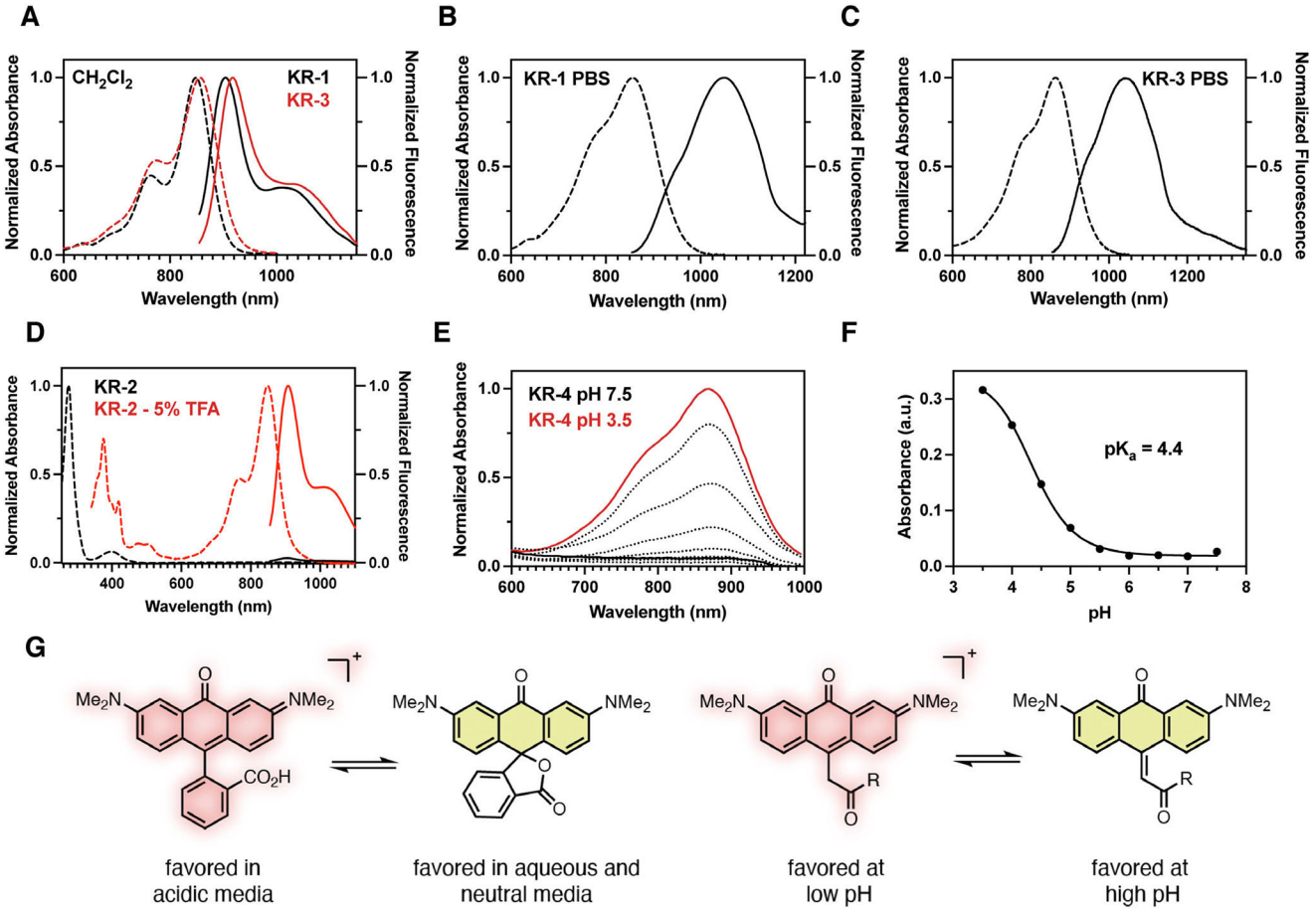

Figure 2.

(A) Normalized absorption (dashed) and emission (solid) data of **KR-1** and **KR-3** in CH_2Cl_2. (B) Normalized absorption (dashed) and emission (solid) data of **KR-1** in PBS pH 7.4. (C) Normalized absorption (dashed) and emission (solid) data of **KR-3** in PBS pH 7.4. (D) Normalized absorption (dashed) and emission (solid) data of **KR-2** in CH_2Cl_2 (black trace) and CH_2Cl_2 supplemented with 5% TFA (red trace). (E) Exo-**KR-4** (250 μM) in PBS buffered from pH 7.5 (black trace) to pH 3.5 (red trace) to generate **KR-4**. (F) Plot of absorbance intensity at λ_{max} = 875 nm *vs* pH; sigmoidal plot fit resulted in apparent pK_a = 4.4.

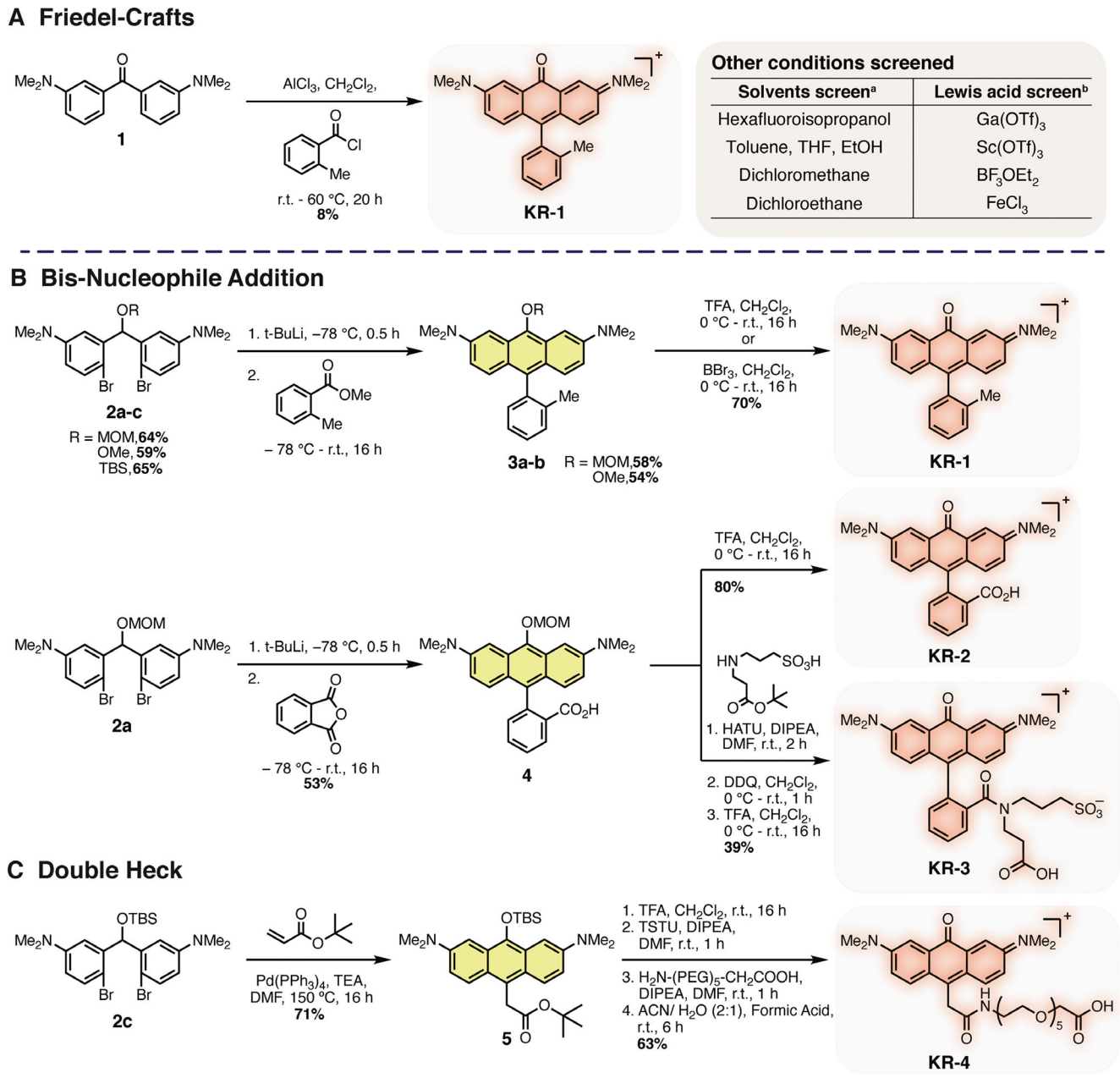

Scheme 1.

(A) Friedel–Crafts approach to **KR-1**. [a](1 eq.), 2-methylbenzoyl chloride (1.1 eq.), $AlCl_3$ (1.75 eq.), solvent (2–2.5 M). [b]1 (1 eq.), 2-methylbenzoyl chloride (1.1 eq.), Lewis acid (1.75 eq.) and CH_2Cl_2 (2 M). (B) Organolithium-mediated approach to **KR-2** and **KR-3**. (C) Double Heck Approach to **KR-4.** See Sections S3 and S4 for detailed synthetic procedures and analysis.

Table 1.

Optical properties measured in dichloromethane (CH_2Cl_2) and in pH 7.4 PBS.

Entry	λ_{abs} (nm) (CH_2Cl_2 / PBS)	λ_{em} (nm) (CH_2Cl_2 / PBS)	ε (M^{-1} cm^{-1}) (CH_2Cl_2 / PBS)	Φ_F (CH_2Cl_2 / PBS)	$\varepsilon \times \Phi_F$ (PBS)	τ_i (ns) (CH_2Cl_2)
Ros*	–/549	–/570	–/72 000	–/0.31	22 320	-
KR-1	855/862	911/1058	28 400/16 500	0.013/0.00013	2.15	0.346
KR-2	848†/–	907†/–	4700/–	0.00029/–	1.36	-
KR-3	855/870	919/1065	15 600/9500	0.0031/0.00017	1.62	-
KR-4	–/874‡	–/1058‡	–/1600‡	-	-	-

*Ref. (62)

†CH_2Cl_2 w/ 5% TFA

‡acetate buffer (0.05 M) pH 3.6. The quantum yield (Q.Y.) of **KR-1** was measured against IR-140 in DMSO as a reference (assuming a Q.Y. of 20%). **KR-1** was used as a standard for subsequent Q.Y. measurements. See Section S5 for additional data and discussion.